Thermal Redistribution of Exciton Population in Monolayer Transition Metal Dichalcogenides Probed with Plasmon–Exciton Coupling Spectroscopy

Tsz Wing Lo,†,# Qiang Zhang,‡,# Meng Qiu,§ Xuyun Guo,† Yongjun Meng,† Ye Zhu,† Jun Jun Xiao,‖ Wei Jin,§ Chi Wah Leung,† and Dangyuan Lei*,†

† Department of Applied Physics, The Hong Kong Polytechnic University, Hong Kong, China

‡ School of Materials Science and Engineering, Harbin Institute of Technology (Shenzhen), Shenzhen 518055, China

§ Department of Electronic Engineering, The Hong Kong Polytechnic University, Hong Kong, China

‖ College of Electronic and Information Engineering, Harbin Institute of Technology (Shenzhen), Shenzhen 518055, China

Abstract

Inversion symmetry breaking and spin–orbit coupling result in spin-splitting of both valence and conduction bands in transition metal dichalcogenide (TMDC) monolayers. The optical transitions between band edges with opposite spins are termed dark excitons that are decoupled with in-plane polarized photons. Here, we find that the presence of dark excitons modifies the temperature-dependent plasmon–bright-exciton coupling strength of a TMDC monolayer interacting with a single plasmonic nanocavity. Quite interestingly, we observe that the modifications are in an opposite manner for WS2 and MoS2 monolayers. Coupled-oscillator analysis reveals that the WS2–nanocavity coupling strength increases with rising temperature, yet that for the MoS2–nanocavity diminishes, which both follow the temperature evolution of the respective exciton oscillator strength obtained by fitting the reflectance spectra of pristine TMDC monolayers with a multi-Lorentz oscillator model. Full-wave electromagnetic simulations with experimentally determined exciton resonance energy and line width at elevated temperatures further reveal a quantitative proportionality between the plasmon–exciton coupling strength and exciton oscillator strength as predicted by a thermal dynamic model. On the basis of these experimental, theoretical, and numerical results, we propose that such a dramatic difference in the temperature-dependent plasmon–bright-exciton coupling strengths is due to the reversed sign of energy difference between the bright and dark excitons in WS2 and MoS2 monolayers, which consequently leads to opposite redistribution of their exciton population (proportional to their oscillator strength) under thermal tuning. Our comparative study provides a unified physics scenario of recent experimental results on the exciton oscillator strengths of these two typical TMDC monolayers, which is of critical importance for fundamental studies such as high-temperature stable polaritons and also for thermally robust photonic applications and nanoscale thermal switching in optical devices.

KEYWORDS:

plasmonic nanocavities transition metal dichalcogenides bright and dark excitons plasmon−exciton coupling thermal tuning

Plasmon–exciton coupling has been attracting a great deal of research interest in studying light–matter interaction in various nanophotonic systems. When the energy exchange rate between a plasmonic nanocavity and coupled excitons exceeds their respective dissipation rates, strong coupling can be reached to produce a hybrid state, called a "plexciton", that possesses partial features of both light and matter excitation. (1−3) The plasmon–exciton strong coupling provides an excellent platform for fundamental physics studies such as Bose–Einstein condensation, (4) quantum entanglement, (3,5,6) and stimulated emission manipulation. (7) It also has many potential applications including single-photon switches, (8) low-threshold lasers, (7) quantum communication, (6) and nonlinear optics. (9) To achieve strong coupling, enhancing coupling strength and reducing decoherence rate are two fundamental requirements. (10) In general, the ratio of quality factor to mode volume quantifies a cavity's capability of enhancing the coupling strength with quantum emitters. Plasmonic nanocavities, which are capable of concentrating light into the subwavelength regime, can significantly boost the light–matter interaction so as to realize strong coupling. Many recent studies have demonstrated the occurrence of strong coupling between a single plasmonic nanocavity and a variety of quantum emitters, such as quantum dots, (11,12) dye molecules, (8,9,13) J-aggregates, (13−16) and transition metal dichalcogenide (TMDC) monolayers. (17−23)

Compared to traditional quantum emitters such as dye molecules and quantum dots, TMDC monolayers exhibit several unusual excitonic properties. Due to the increased quantum confinement and reduced dielectric screening effects, excitons in TMDC monolayers have relatively large binding energies, resulting in fascinating excitonic responses. (24−27) In particular, the inversion symmetry breaking and pronounced spin–orbit coupling induce spin-splitting of both valence and conduction bands (VBs and CBs). (28,29) The spin-splitting of CBs results in two types of neutral excitons with either spin conservation or spin flipping for electronic transitions, (30−35) corresponding to bright and dark excitons in TMDC monolayers, respectively. The bright excitons have pure in-plane dipole moments that can be effectively coupled with in-plane polarized photons. (26) On the contrary, the dark excitons are completely decoupled with in-plane polarized photons, (34−36) and their weak transition dipole moments and the spin flipping requirement make it difficult to probe them with conventional optical spectroscopies.

So far, most TMDC-based plexciton studies have focused on mode optimization of plasmonic nanocavities in order to strengthen the plasmon–exciton interactions, i.e., achieving large Rabi splitting. For example, strong exciton–plasmon coupling was observed in monolayer MoS_2 coupled with an array of silver nanodisks, demonstrating a coupling strength of 58 meV at 77 K. (23) Following that, single plasmonic nanocavities (18−20,22) integrated with TMDC monolayers were used to reach strong coupling at room temperature, with exciton number approaching the quantum limit. While the roles of various plasmon nanocavities have been extensively explored in the context of strong coupling, the exciton properties of TMDC monolayers, such as thermal response and dark excitons, and particularly their effects on plasmon–exciton coupling strength, have been rarely considered. Note that earlier studies on thermal tuning of plasmon–exciton coupling revealed the formation of trion plexcitons (20) and the modification in exciton resonance energy, (22) without explicitly discussing the temperature-dependent WS_2–nanocavity coupling strength, which in fact is crucial for realizing thermally stable strong coupling and exploring high-temperature quantum electrodynamics.

In this article, we demonstrate a comparative temperature-dependent dark-field spectroscopic study on the plasmon–exciton coupling in MoS_2 and WS_2 monolayers, both coupled with single Au@Ag core–shell nanocuboid plasmonic resonators. Coupled oscillator fitting of the measured scattering spectra for both hybrid systems elucidates opposite thermal evolution of their coupling strength, following the same trend of their respective exciton oscillator strength. Combined with experimentally measured temperature-dependent exciton resonance energy and line width, full-wave electromagnetic simulations not only reproduce the measured plasmon–exciton coupling features but also reveal an unambiguous quantitative proportionality of plexcitonic coupling strength and exciton oscillator strength. Considering the reversed energy levels of the bright and dark excitons in MoS_2 and WS_2 monolayers, we attribute such distinctive plexcitonic responses to temperature-induced redistribution of exciton population in the bright and dark excitonic states. Our finding of such anomalous thermal behaviors of TMDC-based plexcitons points out a new direction to design thermally robust nanophotonic devices, suggests a possibility to manipulate polaritons by thermal switching, and also facilitates the design of TMDC-based optoelectronic devices such as fabricating tungsten-based TMDC polariton lasers to prevent self-heating-induced decoupling of polaritons. In addition, our results provide an alternative scheme to study the fine structures of energy levels related to the dark excitons in

TMDC monolayers. Such a scheme utilizes the plasmon–bright-exciton coupling effect rather than directly probing the dark excitons, which can enlarge the sensitivity through the strong light confinement in plasmonic nanocavities.

Many studies have demonstrated the ability of plasmonic nanostructures to facilitate the electromagnetic coupling between exciton and light. (2,37) Here we used a single Au@Ag core–shell nanocuboid as an open plasmonic nanocavity to couple with the excitons in a MoS_2/WS_2 monolayer, as shown in Figure 1(a). Compared to the smooth Au nanorod core, the sharp corners of a nanocuboid structure exhibit stronger local field enhancement and smaller mode volume, both of which can enhance the plasmon–exciton coupling strength. (16) As a matter of fact, such Au@Ag core–shell nanocuboids have plasmonic properties, such as resonance wavelength, dissipation rate, and mode volume, similar to those of silver nanocuboids with the same size and geometry. However, it is challenging to synthesize silver nanocuboids due to the unfavorable anisotropic growth, and thus Au@Ag hybrid core–shell nanocuboids provide a good replacement for silver nanocuboids in various studies and applications. In addition, the plasmon resonance of Au@Ag nanocuboids can be flexibly tuned by simply governing the aspect ratio of the Au core and the thickness of the Ag shell. It promotes the possibility of forming polariton states for matching plasmon resonance with a large range of excitonic resonances in different TMDCs. More importantly, the nanocuboid sustains an in-plane plasmon dipolar mode which provides a strong in-plane local field for efficient coupling with bright excitons in TMDCs. To protect the nanocuboids from sulfurization and thermal deformation under elevated temperatures, we covered the nanocuboids with a 3 nm alumina layer and further separated them from the MoS_2/WS_2 monolayers with a 0.5 nm alumina space layer, as seen in Figure 1(a).

We first examined the temperature-dependent excitonic properties of pristine MoS_2 and WS_2 monolayers and individual Au@Ag nanocuboids. The measured differential reflectance $\Delta R/R_0$ of the MoS_2 and WS_2 monolayers in the energy range of 1.7 to 2.3 eV is shown in Figure S1(a) and (b) as a function of temperature, where R_0 and ΔR correspond to the reflection from a sapphire substrate and the reflection difference between the MoS_2/WS_2 monolayer and the sapphire substrate, (28) respectively. It is seen that the reflectance spectra for the MoS_2 (WS_2) monolayer show two (one) peaks in the measured energy range, which are attributed to the

excitonic absorption of bright A- and B-excitons of MoS_2 (A-exciton only for WS_2). Due to the existence of higher-energy excitonic states, these reflectance peaks are also asymmetric in the considered energy range. By taking a thin-film approximation, the differential reflectance of these TMDC monolayers is found directly proportional to the imaginary part of their dielectric permittivity (see the SI):

$$\frac{\Delta R}{R_0} = -\frac{\pi E}{310} a_{nm} \frac{b}{r_0} \left[\sum_{n=1}^{N} f_n \frac{E_n^2 \Gamma_n E}{(E_n^2 - E^2) + E^2 \Gamma_n^2} \right] \quad (1)$$

where E is the energy in eV, a_{nm} is the thickness of a TMDC layer in units of nm, b and r_0 are simplified terms that depend on the permittivity of sapphire and air (see the SI), and the summation is made for Lorentz oscillators with a number varying from 1 to N. It is noted that the thin-film approximation used in eq 1 is a widely acceptable approximation for studying the optical properties of two-dimensional materials in the visible range as the thickness of TMDC monolayers is in angstrom scale, 3 orders smaller than the wavelength of interest. The reflectance spectra for the MoS_2 (WS_2) monolayer show two (one) peaks in the measured energy range, which are attributed to the excitonic absorption of bright A- and B-excitons of MoS_2 (A-exciton only for WS_2). Due to the existence of higher-energy excitonic states, these reflectance peaks are asymmetric in the considered energy range. Therefore, we fit those MoS_2 (WS_2) spectra in Figure S1(a) (S1(b)) with eq 1 consisting of three oscillators (two oscillators for WS_2) in order to obtain excitonic properties such as exciton energy $E_{A/B}$, line width $\Gamma_{A/B}$, and oscillator strength $f_{A/B}$ for each excitonic state as a function of temperature, with the extracted results shown in Figure S2(a) and (c) for MoS_2 (S2(b) and S2(d) for WS_2). To illustrate the highest possible distribution range of these extracted parameters, the confidence interval of each fitting parameter is also provided in Figure S2 as fitting errors, based on which we can assess the reliability of the corresponding parameters in Figure S2. For example, both the extracted excitonic energy and line width of the WS_2 have smaller fitting errors than those of the MoS_2. This is understandable because more fitting parameters are involved in eq 1 for MoS_2. Similar treatment is applied in all the subsequent fitting results in this work for sensitivity analysis. One can see that the extracted temperature-dependent excitonic energies for both TMDC monolayers can be well described by the O'Donell model: (38)

$$E_{A/B}(T) = E_{A/B}(0) - s\langle\hbar\omega\rangle\left\{\coth\left[\frac{\langle\hbar\omega\rangle}{2k_B T}\right] - 1\right\} \quad (2)$$

where $E_{A/B}(0)$ is the exciton energy at 0 K, s accounts for the exciton–phonon interaction, $\langle\hbar\omega\rangle$ is the average phonon energy, and k_B is the Boltzmann constant. Meanwhile, the extracted line widths follow a linear dependence of temperature T:

$$\Gamma_{A/B}(T) = \Gamma_{A/B}(0) + \alpha T \quad (3)$$

where $\Gamma_{A/B}(0)$ is the intrinsic damping at 0 K and α represents the exciton–phonon coupling strength. (39,40) As can be seen from Figure S2(c) and (d), the extracted temperature-dependent line widths for both TMDC monolayers are also well fitted with eq 3. The well-fitted results based on the theoretical models (eq 2 and eq 3) shown in Figure S2 indicate that the experimentally extracted temperature-dependent excitonic features are reliable, although one may notice that the thermal shifting of the exciton energies are less than or comparable to the exciton line widths. This also confirms that eq 1 is a reasonable multi-Lorentz fitting model that can be used to extract the temperature-dependent excitonic features. From results shown in Figure S2, we can conclude that the bright A- and B-excitons red-shift in energy with rising temperature, accompanied by a pronounced line width broadening. Such a distinctive thermal response of the A- and B-excitons indicates that, upon coupling to a plasmonic nanocavity, the MoS_2 and WS_2 monolayers can be exploited to investigate thermal tuning of plasmon–exciton coupling. On one hand, the observed line width broadening can be attributed to temperature-induced dephasing of the excitonic states due to stronger exciton–phonon coupling at elevated temperatures, (39,40) which can lead to a reduction in the excitonic coherence and thus diminish the plasmon–exciton coupling. On the other hand, the plasmon resonance energy of the Au@Ag nanocuboid is insensitive to temperature variation, but the line width broadens due to increased electron–phonon interaction induced plasmon damping (41) (Figure S3). Transmission electron microscopy (TEM) spectroscopy was performed to characterize the morphology of a typical single Au@Ag nanocuboid (Figure 1(b)) and monitor morphological changes under elevated temperature. Real-time TEM imaging of several Au@Ag nanocuboids reveals unobservable structural deformation or metallic alloying occurring in the interrogated temperature range (Figure S4), consistent with the measured temperature-independent scattering

resonance energy and further evidencing that the observed variation in plasmon damping originates from the intensified electron–phonon interaction.

Upon placing the Au@Ag plasmonic nanocavity on the MoS_2/WS_2 monolayer with a 0.5 nm thick Al_2O_3 spacer as shown in Figure 1(a) and (c), plasmon–exciton coupling occurs and produces two hybridized states with energy ω^+ and ω^-, as manifested by the measured three scattering peaks for MoS_2 in Figure 1(d) and two peaks for WS_2 in Figure 1(e). Clearly, the temperature evolution of the scattering spectra indicates that the plasmon–exciton coupling is significantly tuned by temperature. On the basis of the above observations from the uncoupled plasmonic nanocavity and the pristine MoS_2/WS_2 monolayers, we can conclude that such thermal tuning of the hybrid Au@Ag-MoS_2/WS_2 systems is mainly induced by the thermal sensitivity of the excitonic response in the TMDC monolayer. When the number of excitons interacting with a plasmonic nanocavity exceeds the quantum limit associated with the number of excitons within the cavity mode volume, the plasmon–exciton coupling mechanism, which was originally described by the quantum mechanical Jaynes–Cummings model, can also be precisely interpreted by the classical coupled-oscillator model (COM). (1,19) The validity and accuracy of the COM in describing plasmon–exciton coupling phenomena has been confirmed by many studies. (16−23) The COM contains a radiative plasmon mode and a nonradiative exciton resonance, with their interaction characterized by a coupling strength κ. Here we assume that no direct interexciton coupling occurs between the bright A- and B-excitons at the interrogated temperature regime. (32) The Hamiltonian of coupled oscillators for the plasmon mode with one exciton reads

$$\begin{pmatrix} E_{pl} - i\Gamma_{pl} & \kappa_A \\ \kappa_A & E_A - i\Gamma_A \end{pmatrix} \begin{pmatrix} \alpha \\ \beta \end{pmatrix} = E \begin{pmatrix} \alpha \\ \beta \end{pmatrix} \tag{4}$$

And for the case of two excitons, it becomes

$$\begin{pmatrix} E_{pl} - i\Gamma_{pl} & \kappa_A & \kappa_B \\ \kappa_A & E_A - i\Gamma_A & 0 \\ \kappa_B & 0 & E_B - i\Gamma_B \end{pmatrix} \begin{pmatrix} \alpha \\ \beta \\ \chi \end{pmatrix} = E \begin{pmatrix} \alpha \\ \beta \\ \chi \end{pmatrix} \tag{5}$$

where E_{pl}, E_A, and E_B are the energy of the plasmonic cavity mode and the bright A- and B-excitons of the TMDC monolayer, respectively, and Γ_{pl}, Γ_A, and Γ_B are their corresponding

damping rate. The coupling strengths between the plasmon mode and the A/B-excitons are denoted as κ_A and κ_B, respectively. In eqs 4 and 5, α, β, and χ are the eigenvector components of the coupled system which indicate the fraction of mixing states in the hybrid systems. We use eq 4 to describe the Au@Ag–WS_2 coupling and eq 5 for the Au@Ag–MoS_2 coupling. The fitting of the scattering spectrum is performed with eq S11 in the WS_2 coupled system and eq S12 in the MoS_2 coupled system. The critical parameters of the exciton–cavity coupling can be extracted by fitting the measured scattering spectra with such a COM.

To perform the COM fitting, the energies E_{pl}, E_A, and E_B are set to vary slightly within their experimentally determined ranges (Figure S3(b) for E_{pl}, Figure S2(a) and (b) for E_A and E_B), with justifications provided below. The exact fitting parameter of COM is shown in Tables S1 and S2. Figure 2(a) and (b) show the temperature-dependent A-exciton energy for the MoS_2 and WS_2 monolayers, respectively, extracted from COM fitting of the measured scattering spectra in Figure S5. It is seen that there is an energy shift of about 30 meV (35 meV) for the bright A-exciton (B-exciton) in the MoS_2 monolayer between the energy extracted from the COM fitting (Figure 2(a)) and from the reflectance spectra (Figure S2(a)). For WS_2, the energy shift is about 20 meV (see Figure 2(b) and Figure S2(b)). Such an energy shift can be attributed to the local variation of the excitonic response in the CVD-prepared TMDC samples or to the influence of local doping or local strain induced by the presence of metallic nanostructures. (26) To corroborate the local variation of excitonic response, we have performed PL emission wavelength mapping for a WS_2 monolayer flake.

Although the CVD-grown WS_2 monolayer flake appears highly uniform under bright-field observation (Figure 3(a)), the photoluminescence mapping shown in Figure 3(b) reveals pronounced variation in the emission wavelength. This may arise from defects-related local strain and doping effects. (26) Furthermore, we measured the temperature-dependent scattering spectra of several Au@Ag nanocuboids deposited on several WS_2 monolayer flakes (Figure 3(c)). The Fano dip extracted from the spectra, corresponding to the bright A-exciton resonance energy, varies from 1.99 to 2.03 eV at room temperature. Those experimental results clarify the local variation of exciton energy in a TMDC is the physical origin of the difference between reflectance measurement and COM fitting. Finally, we argue that the presence of an underneath TMDC monolayer could alter, to a certain degree, the plasmon resonance of a supported metallic

nanoparticle, particularly when the optical property of the TMDC monolayer has spatial variation as discussed above. This is because the plasmonic nanocavity—Au@Ag nanocuboid—used in this work has a relatively small mode volume such that it interacts with the underneath TMDC monolayer within an area of only several tens of square nanometers, indicating an extremely sensitive plasmonic response to the local variation of excitonic property. In the COM fitting, the temperature dependence of plasmon damping Γ_{pl} is represented by the linear fit obtained in Figure S3(c) and that of excitonic damping Γ_A and Γ_B by the linear fits in Figure S2(c) for MoS_2 and S2(d) for WS_2. To best fit the measured scattering spectra in Figure 1(d) and (e), a reduction of the excitonic damping determined from the reflectance spectroscopy is necessary to represent the exciton oscillator damping (35 and 10 meV reduction in the A-exciton damping applied for MoS_2 and WS_2, respectively). This required damping reduction could be attributed to geometry-induced excitonic damping and metal-induced dielectric screening in TMDC monolayers by the Au@Ag nanocuboid.

By adopting the above fitting criteria, the coupling strength between the plasmonic cavity mode and the bright A-exciton for both TMDC monolayers is extracted, with results shown in Figure 4(a) and (b). Interestingly, the coupling strengths for MoS_2 and WS_2 demonstrate dramatically different temperature dependence: by heating the hybrid systems from 25 °C to 165 °C, the MoS_2 plexciton coupling strength drops from 31.2 meV to 18.1 meV, while that for the Au@Ag–WS_2 system rises from 36.2 meV to 41 meV. In principle, the vacuum Rabi splitting is defined as $\Omega_{Rabi} = 2\kappa$, which is the energy difference between two adjunct plexcitonic states at zero detuning. Considering the fact that the coupling strength κ in our coupling system is also temperature dependent, we still use $\Omega_{Rabi} = 2\kappa$ to estimate the equivalent temperature-dependent Rabi splitting on the single-particle level. However, we must stress that such equivalent Rabi splitting is different from the real vacuum Rabi splitting since the detuning is not zero in our system. It is possible to obtain the real Rabi splitting value when the plasmon resonance is kept at the same energy as that of the exciton when the temperature is varied, for example by coating the plasmon cavity with dielectric layers of different thicknesses. (19) However, what we are concerned with here is the temperature-induced variation of the polariton coupling strength in the systems rather than their Rabi splitting degree. The small energy difference between the A- and B-excitons in the MoS_2 monolayer induces simultaneous coupling with the same plasmon mode. Focusing on the coupling strength between

the A-exciton and the plasmon mode allows us to specifically study the physical origin of the corresponding temperature dependence. The results of coupling strength shown in Figure 4 indicate that the equivalent Rabi splitting of the plasmon–A-exciton coupling for MoS_2 declines from 62.4 meV at room temperature to 36.2 meV at 165 °C; in sharp contrast, that for WS_2 rises from 72.4 meV to 82 meV. To understand this difference, we note that the temperature-dependent coupling strength κ can be theoretically determined through a semiclassical model: (8)

$$\kappa = \mu \sqrt{\frac{4\pi\hbar N c}{\lambda \varepsilon \varepsilon_0 V}} \tag{6}$$

where μ and N are the transition dipole moment and the number of excitons involved, respectively, V is the mode volume of the plasmonic nanocavity, ε is the dielectric constant of the TMDC monolayer, and the remaining constants are reduced Plank constant $\hbar$, the speed of light in a vacuum c, and the vacuum permittivity ε_0. The mode volume of the plasmonic Au@Ag open cavity and the background dielectric constant of the TMDC monolayers are supposed to be insensitive to thermal variation. (32,42,43) Assuming the transition dipole moment of an exciton is independent of temperature, the plasmon–exciton coupling strength is mainly determined by the temperature-dependent number of involved bright excitons that is proportional to the oscillator strength of the excitonic state concerned, (1)$f \propto N$. Based on the above discussions and eq 6, we can expect that the coupling strength is proportional to the square root of the exciton oscillator strength, i.e., $\kappa \propto f^{1/2}$. To verify this relationship, we first check the coupling strength and exciton oscillator strength of two extreme experimental temperatures of 25 and 165 °C. It is found that the coupling strength ratio κ_{165}/κ_{25} for the MoS_2 (WS_2) plexcitonic system is around 0.58 (1.13), which approaches the value 0.75 (1.06) of the square-root of the oscillator strength ratio, $(f_{165}/f_{25})^{1/2}$. This roughly confirms the consistency between the COM-extracted coupling strength (see Figure 4(a) and (b) for MoS_2 and WS_2, respectively) and reflectance-extracted oscillator strength (see Figure 4(c) and (d) for MoS_2 and WS_2). Although the COM-extracted coupling strength for the plexcitonic system and the Lorentz-model-extracted oscillator strength of the pristine TMDC monolayers can be well correlated with the semiclassical model shown in eq 6, it is still a concern whether the initial approximations, such as temperature-independent excitonic dipole moment and plasmonic mode profile, and the

validity of COM fitting hold true under significant changes in a TMDC's dielectric properties at elevated temperature. Therefore, it is necessary to numerically corroborate the above-observed correlation between exciton oscillator strength and plexcitonic coupling strength under thermal tuning. To this end, we numerically investigate the plasmon–exciton coupling in the Au@Ag–WS_2/MoS_2 systems by simulating their scattering spectra as a function of elevated temperature. In the simulations, the geometry and size parameters of the Au@Ag nanocuboid are obtained from TEM imaging with slight modification accounting for size fluctuation in order to best match the measured scattering spectra. Without loss of generality, in the simulations we consider only the changes in the excitonic response of the TMDC monolayers under rising temperature and neglect the temperature-induced plasmon damping in the Au@Ag nanocuboids. This simplification is rational because the temperature-induced plasmon damping is a common feature in both the WS_2- and MoS_2-based coupling systems, which would not result in the opposite tendency of coupling strength as a function of temperature. In addition, fixing the plasmonic response of the nanoparticle avoids introducing more variables in the COM fitting, thereby allowing a clear understanding of the excitonic response of the TMDCs under different temperatures. The anisotropic permittivity of monolayer WS_2 (MoS_2) (44) was modeled with a constant out-of-plane component ε_{out} and a temperature-dependent in-plane component $\varepsilon_{in}(E, T)$ described respectively by a single-pole and a double-pole Lorentz oscillator term:

$$\varepsilon_{in}(E, T) = \varepsilon_{\infty} + \frac{f_A(T)\, E_A^2(T)}{E_A^2(T) - E^2 - i\Gamma_A(T)E} \tag{7a}$$

$$\varepsilon_{in}(E, T) = \varepsilon_{\infty} + \frac{f_A(T)\, E_A^2(T)}{E_A^2(T) - E^2 - i\Gamma_A(T)E} + \frac{f_B(T)\, E_B^2(T)}{E_B^2(T) - E^2 - i\Gamma_B(T)E} \tag{7b}$$

where $E_{A/B}(T)$ are the exciton resonance energies of the bright A- and B-excitons, $f_{A/B}(T)$ the corresponding oscillator strength, and $\Gamma_{A/B}(T)$ the corresponding exciton line width. Equation 7 models the pure in-plane excitonic response nature of a monolayer TMDC.

With the above-described anisotropic permittivity of monolayer WS_2, we first make a virtual control simulation to calculate scattering spectra for the Au@Ag–WS_2 system by varying the exciton oscillator strength (f_A) yet fixing all the other parameters (E_A = 2.024 eV and Γ_A = 0.055 eV, corresponding to the measured values for the pristine monolayer WS_2 at 25 °C). By fitting the simulated scattering spectra with the same COM used for fitting the experimental spectra, we

can extract the corresponding plexcitonic coupling strength as a function of the exciton oscillator strength, which indeed obeys the relationship $k \propto f^{1/2}$ as shown in Figure S6. Then, we consider the temperature dependence of exciton energy and damping rate in the anisotropic permittivity of monolayer TMDCs as described by eq 7. Here, $E_{A/B}(T)$ are given by O'Donell's model (eq 2) in Figure S2(a) and (b) with a constant energy shift $\Delta E_{A/B}$ accounting for the local variation in exciton energy, and $\Gamma_{A/B}(T)$ follows the linear temperature dependence given by eq 3. The parameter $f_{A/B}$ for WS_2 (MoS_2) was given by a liner fit of the exciton oscillator strength extracted from the measured differential reflectance spectra in Figure 4(c) and (d). The exact parameters for the permittivity of monolayer WS_2 and MoS_2 used in the numerical simulations are listed in Table 1. Note that $\Gamma_{A/B}(0)$ for monolayer WS_2 is negative since the linear dependence model neglects the excitonic line width's nonlinear dependence on temperature, which shows a minor effect in room-temperature conditions. (39) Applying these parameters given in Table 1 ensures that the temperature-dependent excitonic responses in the simulation models are consistent with the experiments.

The simulated temperature-dependent scattering spectra for the two coupled systems shown in Figures 5(a) and 6(a) agree well with the measured experimental spectra in Figure 1(e) and (d), respectively. Next, we fit the simulated spectra with COM to extract the plasmon–A-exciton coupling strength as a function of temperature. In the COM fitting, the plasmon resonance energy of the Au@Ag nanocavity mode E_{pl} and its corresponding damping rate Γ_{pl} are fixed respectively to be 2.007 eV for the Au@Ag–WS_2 system (1.957 eV for Au@Ag–MoS_2) and 0.235 eV for both cases to best fit the simulated temperature-dependent scattering spectra, while the exciton resonance energy $E_{A/B}(T)$ and damping rate $\Gamma_{A/B}(T)$ are given by eqs 2 and 3, respectively, with relevant parameters listed in Table 1. Clearly, the COM-extracted coupling strength for WS_2 (see Figure 5(b)) gradually increases with elevating the temperature, while that for MoS_2 (Figure 6(b)) decreases, both agreeing well with the experimental results in Figure 4(b) and (a). Interestingly, the ratio of the coupling strength to the square root of the oscillator strength for both systems are constant, as shown in the insets of Figures 5(b) and 6(b), consistent with the prediction by eq 6. This verifies the direct correlation between exciton oscillator strength and plasmon–exciton coupling strength. Moreover, the COM-extracted coupling strengths from the temperature-dependent scattering spectra for the Au@Ag–WS_2 plexcitonic system (Figure 5(a)) only show a very small deviation from that extracted values from the

control simulation (Figure S6), indicating that the influences of the temperature-induced variations in exciton energy and damping rate on the COM fitting are negligible. This further supports the robust relationship of $k \propto f^{1/2}$ between plexcitonic coupling strength and exciton oscillator strength, which would not be affected by limited variations in other fitting parameters. At the same time, k would usually have a larger signal-to-noise ratio than f since the optical responses of excitons are enhanced by plasmonic modes in plexcitonic systems. Therefore, the coupling strength k in a plexcitonic system can be used as an ideal parameter to represent the variation of exciton oscillator strength f.

In addition to the above-discussed spectroscopic features, the strong plexcitonic coupling in both systems also has pronounced footprints in their near-field intensity profiles at coupling resonances P_1, D_1, and P_2, as shown in Figures 5(c) and 6(c). At each resonance, the large in-plane background dielectric permittivity of monolayer TMDC induces image charges that couple to the localized surface plasmons of the Au@Ag nanocuboid itself, enhancing the local field intensity at the cuboid corners in contact with the TMDC monolayer and thus amplifies the plasmon–exciton coupling effect. Overall, the near-field intensity at the Fano resonance dip D_1 is weaker than that at the split plasmon resonance peaks P_1 and P_2, due to the near-field quenching effect induced by the cavity-enhanced exciton conductance. (45)

After verifying the rationality of our COM fitting and numerical study, exploiting the anomalous thermal dependence of COM-extracted oscillator strengths for both MoS_2 and WS_2 is the focus of this study. In general, the optical response of a simplified two-level quantum mechanics system depends on densities of both the ground and excited states. (46,47) Under weak-field approximation, the light-driven density variation in the ground state should be relatively small such that we just need to consider the density changing of the excited state. In this case, the semiclassical oscillator strength of the bright A-exciton for TMDC monolayers is proportional to the exciton density N/V, exciton resonance energy E_0, and transition dipole moment μ, i.e., $f \propto NE_0\mu/V$, which jointly determine the temperature dependence of the exciton oscillator strength. (1) Specifically, increasing the temperature can result in a reduction of N and E_0 due to enhanced thermal dissociation of excitons and exciton–phonon interaction (less than 4% red-shift in E_0 when increasing the temperature from 25 °C to 165 °C), respectively. Therefore, we expect a slight drop in the exciton oscillator strength at elevated temperatures. However, this physical

picture cannot explain the above-observed totally different temperature dependences for the bright A-exciton oscillator strength for WS_2 and MoS_2 as well as the corresponding plexcitonic coupling strength, i.e., gradually increased oscillator strength for the former (about 10% increase for the same temperature variation) yet rapidly decreased oscillator strength for the latter (more than 30% decrease).

To fully understand such unusual temperature dependences of the bright A-exciton oscillator strength in WS_2 and MoS_2, we have to take into account the presence of dark excitons in both systems, which lie around the respective bright exciton state with an energy difference typically of a few tens of meV. (30,34,35,48) These dark excitons decouple from in-plane polarized photons and can only weakly couple with out-of-plane polarized photons, (36) thereby leading to negligible optical transition in comparison with the bright excitons (as schematically represented by the green arrows in Figure 7). Therefore, the dark excitons cannot directly couple with the in-plane plasmon mode in our system. However, the population density of bright excitons is affected by presence of dark excitons because the redistribution of their population is correlated under thermal tuning, as will be discussed in detail later. This indicates that the existence of dark excitons modifies the coupling strength between bright excitons and the in-plane plasmon mode in an indirect way. Such indirect impact of the dark excitons on the plasmon–bright-exciton coupling has naturally been incorporated in the COM through modeling the temperature-dependent oscillator strength of the bright excitons. As a result, the scattering responses of the plasmon–bright-exciton coupling system can be well fitted by the COM without considering dark excitons as additional oscillators. Considering the small energy difference between the bright and dark excitonic states and the average thermal energy ranging from 26 meV at 25 °C to 38 meV at 165 °C in our experiment, the thermal-assisted transitions between those states can be quite intense (as illustrated by the purple arrows in Figure 7), which reaches an ultimate thermal equilibrium after fast redistribution of excitonic population. Assuming that the bright and dark excitonic states form a quasi-two-level system, they should follow the two-level Boltzmann distribution as $N_H = N_0 \exp(-\Delta E/k_B T)/(\exp(-\Delta E/k_B T) + 1)$ for the higher occupied energy level and $N_L = N_0/(\exp(-\Delta E/k_B T) + 1)$ for the lower occupied energy level. Here N_0 is the total number of photoexcited excitons, which is proportional to the incident light intensity and the transition dipole moment between the ground state and the bright excitonic state. Similar analysis of the thermal distribution of excitonic states was demonstrated in a previous study on time-resolved

photoluminescence in monolayer WSe_2. (48) Under rising temperature, the Boltzmann distribution indicates an increase of density in the higher-energy exciton state and a corresponding decrease in the density of the lower-energy exciton state. Earlier studies found that the dark exciton of monolayer MoX_2 (X = S or Se) has a higher energy than the bright exciton (30,48) (see left panels of Figure 7(a) and (b)), while that of the WX_2 has a lower energy than the bright exciton (30,48) (see right panels of Figure 7(a) and (b)). As a result, the bright excitons in MoS_2 lose oscillator strength, while those in WS_2 gain oscillator strength with rising temperature. This physical model qualitatively agrees with our experimental results and also provide a unified physical picture to explain previous studies on temperature-dependent oscillator strengths of MoS_2, (44) $MoSe_2$, (43) WS_2, (20) and WSe_2. (42)

By fitting the temperature-dependent coupling strength of the Au@Ag/WS_2 coupling system given in Figure 4(b) with a two-level Boltzmann distribution, $N_H = N_0 \exp(-\Delta E/k_B T)/(\exp(-\Delta E/k_B T) + 1$, we are able to roughly estimate the energy difference between the dark and bright excitons of WS_2. As shown in Figure S7, the energy difference extracted from the model is 27 meV, which is half of the reported value (54 meV (36)). The deviation between the extracted energy difference and the reported value may originate from a possible coupling effect between the bright exciton state and other excitonic states. Using the extracted energy difference, it is possible to estimate the percentage change of the plasmon–exciton coupling strength induced purely by the redistribution of excitonic population. In the temperature range from 25 to 165 °C, our model reveals a coupling strength variation of 12.4% using the extracted energy difference, which in fact is significantly smaller than the variation of 32.7% for the reported energy difference of 54 meV. This tells us that the weight of the Boltzmann factor in the coupling strength variation can change even more drastically than we have estimated from the model. It is noted that, since the energy difference between the two excitonic states is obtained by fitting the COM-extracted temperature-dependent coupling strength, it may cause the issue of error transferring. This could be one possible reason for the deviation of our Boltzmann model extracted energy difference from the experimentally determined value at low temperature. (36)

Note that in our model, for simplicity, we exclude the consideration of charged exciton states (such as trion state) in discussing the thermal tendency of exciton distribution. This is because

the trion state in both WX_2 and MoX_2 monolayers has a lower energy than the bright exciton, the presence of which would strengthen the bright exciton population in both systems under rising temperature, inconsistent with the observed opposite thermal dependences of exciton oscillator strength and plexcitonic coupling strength for WS_2 and MoS_2. To favor the existence of trion states at room temperature or even higher temperature, significant doping of TMDC monolayers through electrical gating, chemical doping, or optical pumping is necessary. In our experiment, none of those doping mechanisms were applied. Nevertheless, more comprehensive studies are required for quantitatively understanding the oscillator strength distribution with temperature variation in TMDC monolayers.

In conclusion, we studied the temperature dependences of the plexcitonic coupling strength in MoS_2/WS_2 monolayers respectively hybridized with a single plasmonic open nanocavity. Using a coupled-oscillator model, we found opposite tendencies of the coupling strength for the two plexcitonic systems, consistent with the temperature evolution of the bright A-exciton oscillator strength of pristine MoS_2/WS_2. Using experimentally determined parameters, full-wave simulations well reproduced the measured scattering spectra of the two coupled systems and revealed a constant ratio of the plexcitonic coupling strength to the square root of the exciton oscillator strength as predicted by a quantum mechanical model. On the basis of the experimental and numerical results, we proposed a physically phenomenological model in which the reversed energy difference between the bright and dark excitons in the two TMDC monolayers leads to opposite redistribution of excitonic population to those exciton states under assistance by considerable thermal excitation energy at elevated temperatures. This consequently contributes to decreased oscillator strength in MoS_2 yet increased oscillator strength in WS_2, providing a unified physical explanation of recently reported temperature-dependent oscillator strengths of MoX_2 and WX_2. Our results not only offer new insights for understanding the thermal response of cavity–exciton strong coupling but also point out the critical role of dark excitonic states in affecting the plasmon–bright-exciton coupling strength. We stress that the opposite redistribution of excitonic population under thermal tuning is essentially determined by the inherent excitonic property of MoX_2 and WX_2 monolayers and does not depend on the plasmonic property of specific metallic nanostructures used in the coupling system. It is expected that the thermal tuning of plasmon–bright-exciton coupling features can be used to study the fine structures of the energy level of TMDC monolayers. For example, it is possible to determine the dark exciton

energy more precisely if we can further improve the plasmon–bright-exciton coupling strength by utilizing plasmon nanocavities with higher quality factors and smaller model volumes.

Methods

Sample Preparation

MoS_2 and WS_2 monolayer samples were grown on sapphire substrate through a chemical vapor deposition (CVD) technique (Carbon Six Ltd.). Au@Ag core–shell nanocuboids covered with a surfactant layer of CTAB were purchased from Nanoseedz Ltd. An Al_2O_3 layer of 0.5 nm thick was deposited on the MoS_2 and WS_2 monolayers with atomic layer deposition (ALD) to prevent possible chemical reaction and charge transfer between the Au@Ag nanocuboids and TMDC monolayers. (19) The Au@Ag nanocuboids in 1OD (optical density per centimeter light path of largest resonance) aqueous solution were spin-coated on the TMDC monolayers first at 100 rpm for 60 s to obtain a uniform distribution of aqueous solution and then at 3000 rpm for 30 s to remove excess solution. Finally, an extra layer of 2 nm thick Al_2O_3 was deposited on the TMDC–Al_2O_3–Au@Ag sample to eliminate oxidation in ambient and morphology variation under high temperature. (49) The thicknesses of Al_2O_3 layers were monitored by controlling the reactor temperature (85 °C) and the number of duty cycles (8 cycles for 0.5 nm thickness and 26 cycles for 2 nm thickness).

Optical Spectroscopy

Differential reflectance spectroscopy of TMDC monolayers and dark-field scattering spectroscopy of individual Au@Ag nanocuboids were performed with a custom-built microspectroscopy system. In the differential reflectance measurements, a 10× magnification bright-field objective (NA = 0.3) focused an unpolarized white-light beam from an incandescent lamp onto the TMDC monolayers at near-normal incidence. The reflected light signal was collected by the same objective and directed to a monochromator (Princeton Instrument, SP2300) coupled with a silicon CCD (Princeton Instrument, PIXIS: 400BR eXcelon) through a tube lens focusing system. A slit at the monochromator entrance was used to block unwanted signal so as to achieve signal collection from a desired microscale area. To avoid reflectance from the surface of the sample stage, samples were stuck on a carbon tab to absorb the transmitted light. In the scattering measurements, individual Au@Ag nanocuboids were illuminated at large tilting angle

by an unpolarized white-light beam from an incandescent lamp through a dark-field objective condenser (100×, NA = 0.8). The backscattered light signal was collected by the same objective and coupled to the spectrometer through the same scheme as the reflectance measurements. An electronically controlled heating stage was integrated with the dark-field microscope system for raising the temperature at a tuning step of 10 °C. Each tuning step was held for 3 min to ensure the entire sample reached steady temperature before carrying out spectroscopic measurements.

Numerical Simulations

The plasmon–exciton coupling in the Au@Ag–TMDC plexcitonic systems was numerically studied as a function of temperature with the finite element method implemented in a commercial software package (COMSOL Multiphysics 4.3a, radio frequency module). A standard two-step process was adopted in computing the far-field response of a single Au@Ag nanocuboid coupled to the TMDC monolayer. In the first step, the full field was computed for the TMDC–nanoparticle hybridized system in the absence of the Au@Ag nanocuboid, illuminated by a plane wave at normal incidence. The field obtained from the first step was then used as the background fields to calculate the scattered fields of the coupled system in the second step. The scattered power flux of the coupled system was collected within a solid angle of 106° (corresponding to the objective NA 0.8 used in the dark-field scattering measurements) to obtain the totally measurable scattering response. (50) The thickness of monolayer WS_2 (MoS_2) was modeled as 0.62 nm (0.65 nm) (21) with temperature-dependent excitonic properties. To properly mesh such thin layers, we apply a transformation optics approach to scale the WS_2 (MoS_2) thickness to 6.2 nm (6.5 nm) with corresponding modifications to its permittivity and permeability. The permittivity data of silver and gold were adopted from the empirical data given by Johnson and Christy. (51) The permittivity of sapphire and alumina were considered nondispersive and set as 3.13 to simplify the slight optical anisotropy of sapphire crystal.

ASSOCIATED CONTENT

Supporting Information

The Supporting Information is available free of charge on the ACS Publications website.

Derivation of eq 1 based on the transfer matrix method, COM fitting equations and parameters of plexciton systems, more data and details on the temperaturedependent responses of TMDC monolayers, Au@Ag cuboids and their coupled structures, results of control simulation on the Au@Ag−WS2 system, and extracting energy difference between two states by a two-level Boltzmann fitting model (PDF)

AUTHOR INFORMATION

Corresponding Author *E-mail: dangyuan.lei@polyu.edu.hk.

Author Contributions # T. W. Lo and Q. Zhang contributed equally to this work.

Notes

The authors declare no competing financial interest.

ACKNOWLEDGMENTS

We acknowledge the financial support by the Hong Kong Research Grants Council (GRF Grant No. 15303718 and ECS Grant No. 25301617), the Hong Kong Polytechnic University (Grant Nos. G-SB82 and 1-ZVG4), and the China Postdoctoral Science Foundation (2018M630356).

Graphical image

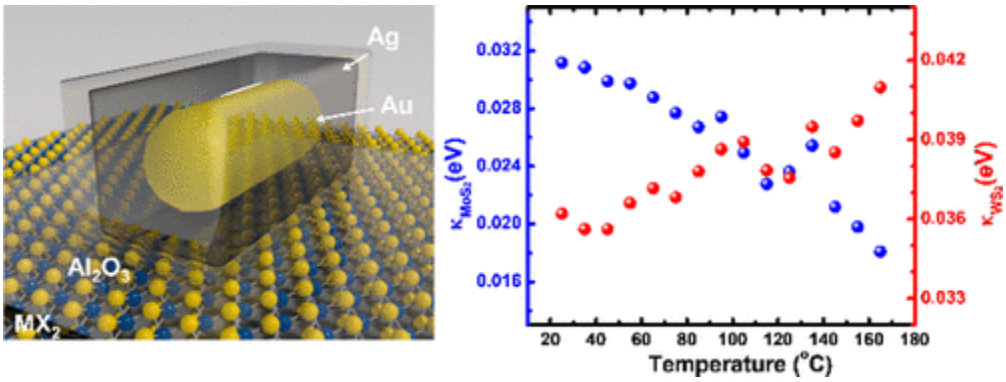

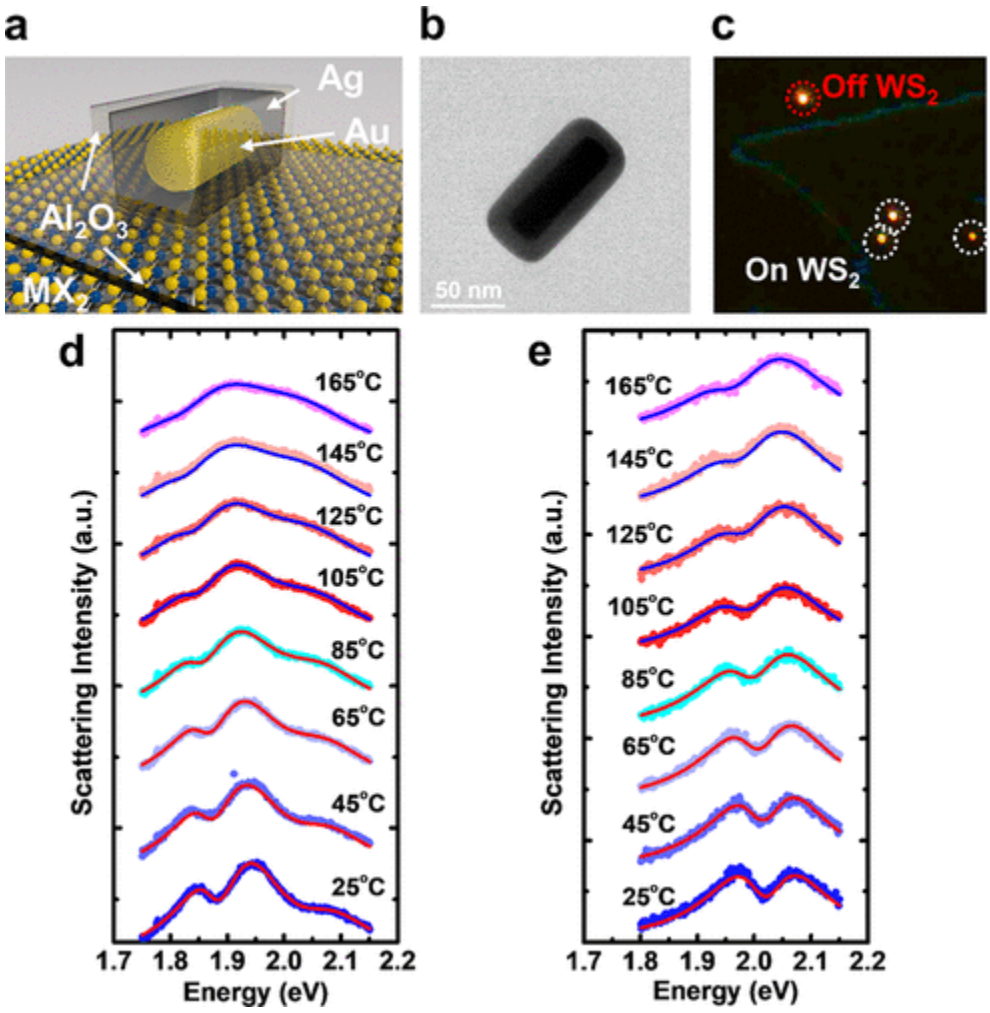

Figure 1. (a) Schematic diagram of a single Au@Ag nanocuboid separated from a TMDC monolayer by a thin Al_2O_3 layer, with the whole system covered by another Al_2O_3 layer. (b) TEM image of a Au@Ag nanocuboid. The scale bar is 50 nm. (c) Dark-field optical image of Au@Ag nanocuboids on a WS_2 monolayer flake. (d, e) Measured temperature-dependent scattering spectra of a single Au@Ag nanocuboid on a MoS_2 (d) and WS_2 (e) monolayer flake, respectively. Symbols represent experimental results, and lines are fitting results by a coupled-oscillator model.

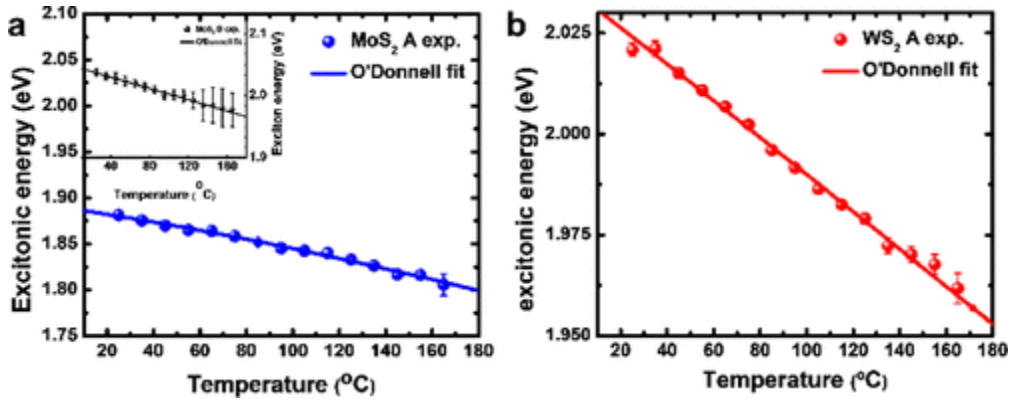

Figure 2. Temperature-dependent A-exciton energy for (a) MoS_2 and (b) WS_2 monolayers, both extracted from COM fitting of the measured scattering spectra in Figure S5. The insert in (a) shows the extracted B-exciton energy for MoS_2. Solid lines represent the fitting curves of exciton energies as a function of temperature by the O'Donnell model.

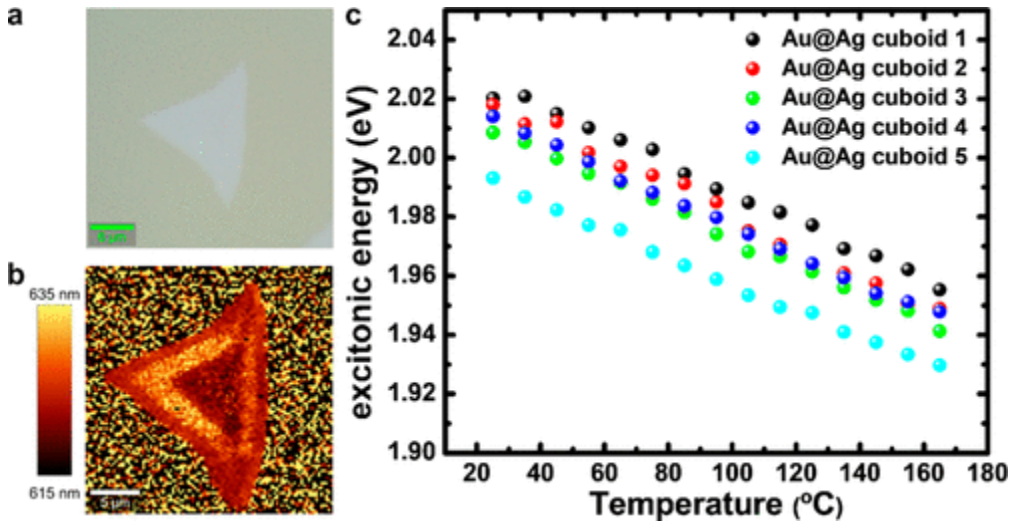

Figure 3. (a) Bright-field optical image of a WS_2 monolayer flake captured with a 100× objective (NA 0.9). (b) Photoluminescence mapping of the same flake under excitation of a 532 nm CW laser with the same objective as (a). (c) A-exciton energy of a WS_2 monolayer extracted from COM fitting of scattering spectra of five different Au@Ag nanocuboids on a WS_2 monolayer flake

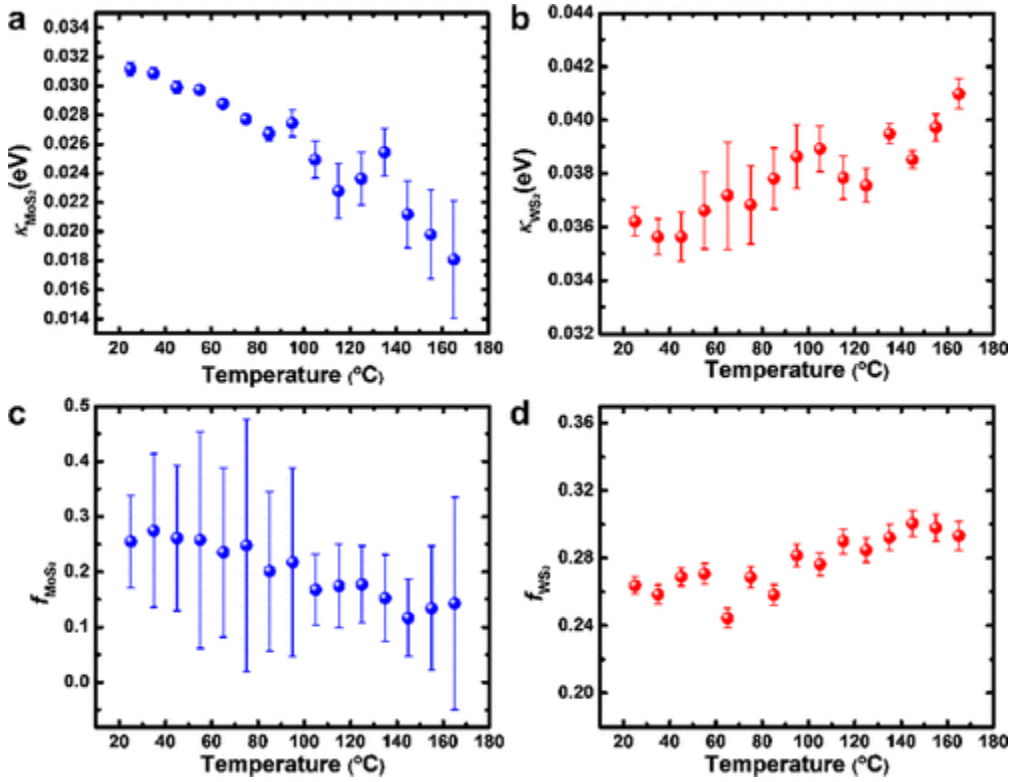

Figure 4. (a, b) COM-extracted coupling strengths for the Au@Ag–MoS_2 (a) and Au@Ag–WS_2 (b) hybrid systems, respectively. (c, d) Lorentz-model-extracted oscillator strengths for the bright A-exciton in the MoS_2 (c) and WS_2 (d) monolayers under rising temperature, respectively.

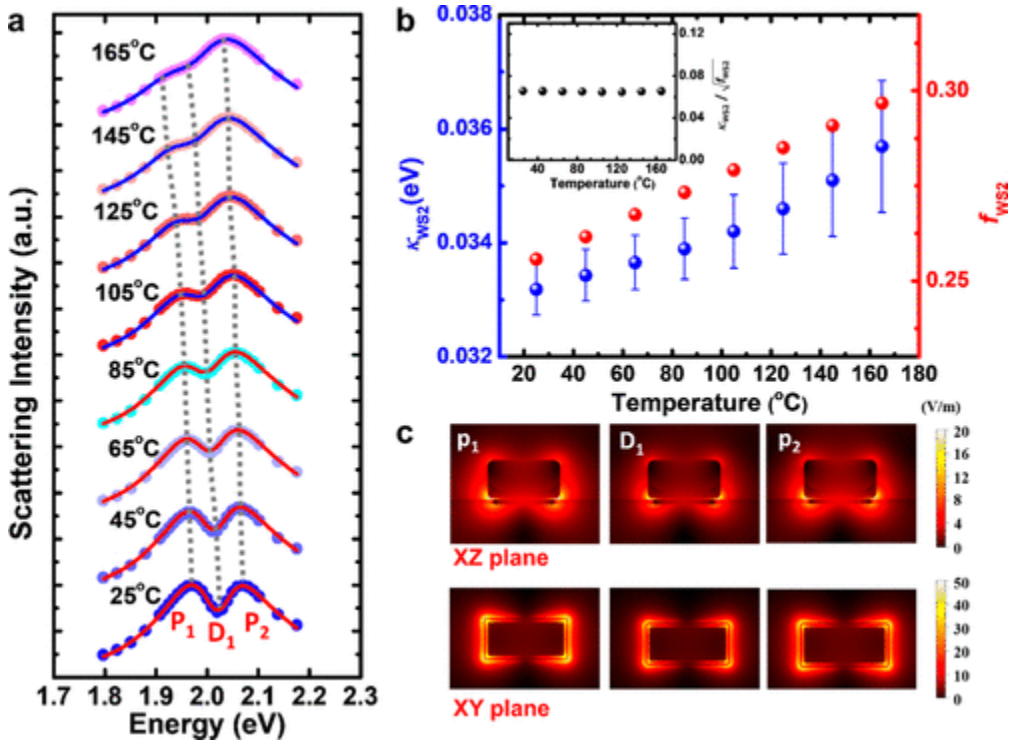

Figure 5. (a) Simulated temperature-dependent scattering spectra for a single Au@Ag nanocuboid coupled to a WS_2 monolayer. (b) COM-fit-extracted coupling strength for the Au@Ag–WS_2 plexcitonic system as a function of temperature (blue dots). The A-exciton oscillator strength of WS_2 (red dots) was obtained by a linear fit of the experimental results in Figure 4(d). The inset plots the ratio of the COM-fit-extracted coupling strength to the square root of the oscillator strength. (c) Simulated local-field distribution in the coupled system at resonances P_1, D_1, and P_2 as marked in (a), with the upper panel showing the *xz*-plane view and the bottom panel the *xy*-plane view.

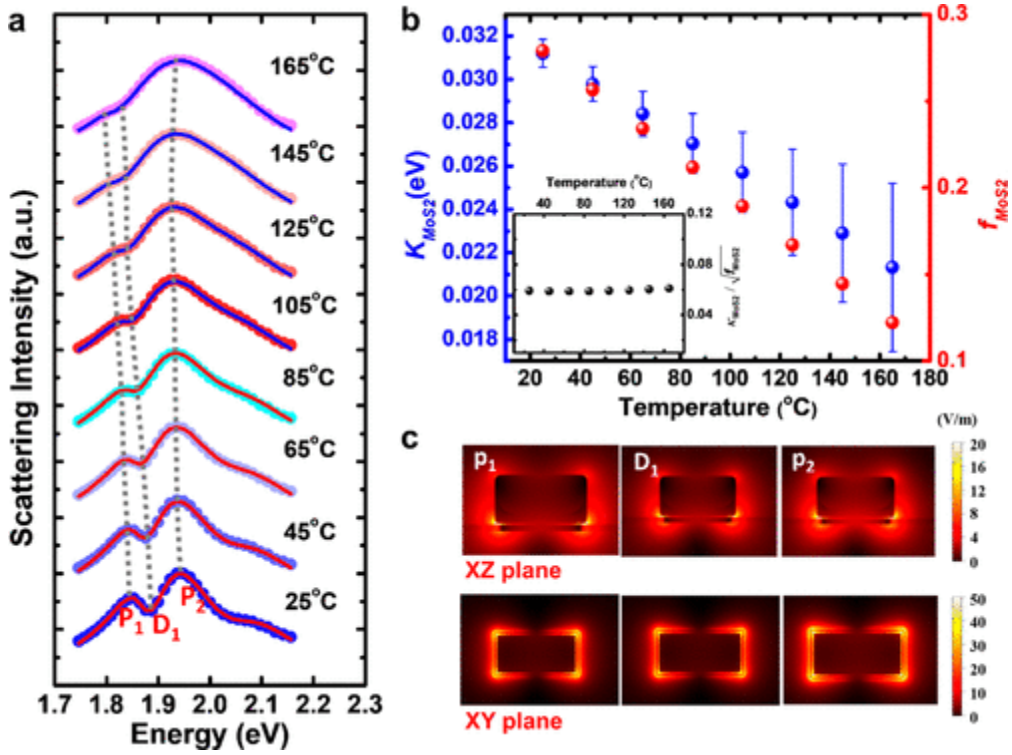

Figure 6. Similar simulation results to Figure 5 for a single Au@Ag nanocuboid coupled to a MoS_2 monolayer.

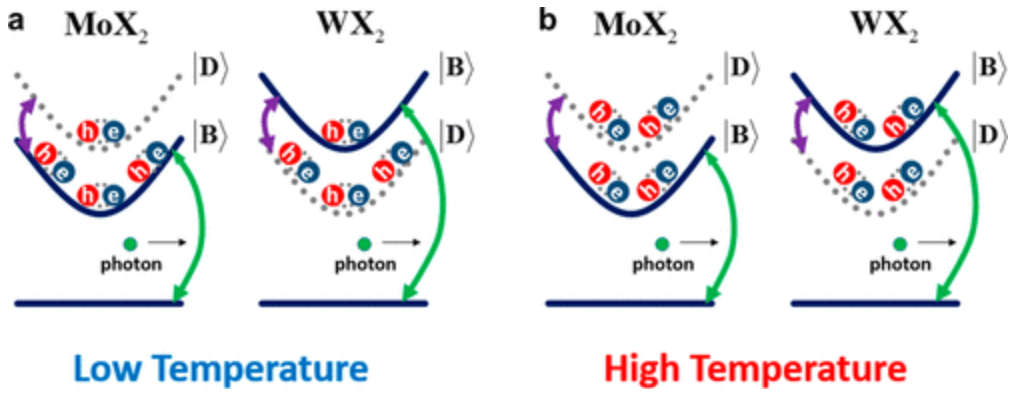

Figure 7. (a, b) Schematic diagrams of exciton densities of MoX_2 and WX_2 at low (a) and high (b) temperature. Solid black lines represent bright exciton states and gray dotted lines the dark exciton states. Solid green arrows represent the exciton radiation that can couple with plasmons. Solid purple arrows represent thermally induced transitions. Under rising temperature, the oscillator strength redistributes from low- to high-energy excitonic states, which consequently alters the density of bright exciton states coupled to the plasmonic nanocavity.

Table 1. Simulation Parameters for Modeling the Permittivity of Monolayer WS_2 and MoS_2

TMDC	ε_{out}	ε_{∞}	$E_{A/B}(0)$ [eV]	$s_{A/B}$	$\langle h\omega \rangle_{A/B}$ [eV]	$\Gamma_{A/B}(0)$ [eV]	$\alpha_{A/B}$	$\Delta E_{A/B}$[eV]
WS_2	2.9	17.7	2.024	3.47	0.063	-0.064	$4 \times 10{-}4$	0.0214
MoS_2	2.8	21	1.89/2.02	3.15/7.61	0.06/0.111	0.091/1.38	$1.38 \times 10{-}4$ /$7.42 \times 10{-}4$	0.03/0.037

REFERENCES

(1) Törmö, P.; Barnes, W. L. Strong Coupling between Surface Plasmon Polaritons and Emitters: A Review. Rep. Prog. Phys. 2015, 78 (1), 013901.

(2) Hugall, J. T.; Singh, A.; vanHulst, N. F. Plasmonic Cavity Coupling. ACS Photonics 2018, 5 (1), 43−53.

(3) Fitzgerald, J. M.; Narang, P.; Craster, R. V.; Maier, S. A.; Giannini, V. Quantum Plasmonics. Proc. IEEE 2016, 104 (12), 2307− 2322.

(4) Kasprzak, J.; Richard, M.; Kundermann, S.; Baas, A.; Jeambrun, P.; Keeling, J. M. J.; Marchetti, F. M.; Szymanska, M. H.; Andre´ , R.;´ Staehli, J. L.; et al. Bose−Einstein Condensation of Exciton Polaritons. Nature 2006, 443 (7110), 409−414.

(5) Kimble, H. J. The Quantum Internet. Nature 2008, 453 (7198), 1023−1030.

(6) Sillanpaä, M. A.; Park, J. I.; Simmonds, R. W. Coherent¨ Quantum State Storage and Transfer between Two Phase Qubits via a Resonant Cavity. Nature 2007, 449 (7161), 438−442.

(7) Kena-Cohen, S.; Forrest, S. R. Room-Temperature Polariton´ Lasing in an Organic Single-Crystal Microcavity. Nat. Photonics 2010, 4 (6), 371−375.

(8) Chikkaraddy, R.; DeNijs, B.; Benz, F.; Barrow, S. J.; Scherman, O. A.; Rosta, E.; Demetriadou, A.; Fox, P.; Hess, O.; Baumberg, J. J. Single-Molecule Strong Coupling at Room Temperature in Plasmonic Nanocavities. Nature 2016, 535 (7610), 127−130.

(9) Nan, F.; Zhang, Y. F.; Li, X.; Zhang, X. T.; Li, H.; Zhang, X.; Jiang, R.; Wang, J.; Zhang, W.; Zhou, L.; et al. Unusual and Tunable One-Photon Nonlinearity in Gold-Dye Plexcitonic Fano Systems. Nano Lett. 2015, 15 (4), 2705−2710.

(10) Marquier, F.; Sauvan, C.; Greffet, J. J. Revisiting Quantum Optics with Surface Plasmons and Plasmonic Resonators. ACS Photonics 2017, 4 (9), 2091−2101.

(11) Santhosh, K.; Bitton, O.; Chuntonov, L.; Haran, G. Vacuum Rabi Splitting in a Plasmonic Cavity at the Single Quantum Emitter Limit. Nat. Commun. 2016, 7, 11823.

(12) Hennessy, K.; Badolato, A.; Winger, M.; Gerace, D.; Atatüre, M.; Gulde, S.; Falt, S.; Hu, E. L.; Imamog¨ ˘lu, A. Quantum Nature of a Strongly Coupled Single Quantum Dot-Cavity System. Nature 2007, 445 (7130), 896−899.

(13) Thomas, R.; Thomas, A.; Pullanchery, S.; Joseph, L.; Somasundaran, S. M.; Swathi, R. S.; Gray, S. K.; Thomas, K. G. Plexcitons: The Role of Oscillator Strengths and Spectral Widths in Determining Strong Coupling. ACS Nano 2018, 12, 402−415.

(14) Zengin, G.; Wersall, M.; Nilsson, S.; Antosiewicz, T. J.; Ka¨ ll,¨ M.; Shegai, T. Realizing Strong Light-Matter Interactions between Single-Nanoparticle Plasmons and Molecular Excitons at Ambient Conditions. Phys. Rev. Lett. 2015, 114, 157401.

(15) Stete, F.; Koopman, W.; Bargheer, M. Signatures of Strong Coupling on Nanoparticles: Revealing Absorption Anticrossing by Tuning the Dielectric Environment. ACS Photonics 2017, 4 (7), 1669−1676.

(16) Liu, R.; Zhou, Z. K.; Yu, Y. C.; Zhang, T.; Wang, H.; Liu, G.; Wei, Y.; Chen, H.; Wang, X. H. Strong Light-Matter Interactions in Single Open Plasmonic Nanocavities at the Quantum Optics Limit. Phys. Rev. Lett. 2017, 118, 237401.

(17) Lundt, N.; Klembt, S.; Cherotchenko, E.; Betzold, S.; Iff, O.; Nalitov, A. V.; Klaas, M.; Dietrich, C. P.; Kavokin, A. V.; Höfling, S.; et al. Room-Temperature Tamm-Plasmon Exciton-Polaritons with a WSe2 monolayer. Nat. Commun. 2016, 7, 12613.

(18) Kleemann, M. E.; Chikkaraddy, R.; Alexeev, E. M.; Kos, D.; Carnegie, C.; Deacon, W.; DePury, A. C.; Große, C.; DeNijs, B.; Mertens, J.; et al. Strong-Coupling of WSe2 in Ultra-Compact Plasmonic Nanocavities at Room Temperature. Nat. Commun. 2017, 8, 13328.

(19) Zheng, D.; Zhang, S.; Deng, Q.; Kang, M.; Nordlander, P.; Xu, H. Manipulating Coherent Plasmon-Exciton Interaction in a Single Silver Nanorod on Monolayer WSe2. Nano Lett. 2017, 17 (6), 3809− 3814.

(20) Cuadra, J.; Baranov, D. G.; Wersall, M.; Verre, R.; Antosiewicz,¨ T. J.; Shegai, T. Observation of Tunable Charged Exciton Polaritons in Hybrid Monolayer WS2- Plasmonic Nanoantenna System. Nano Lett. 2018, 18 (3), 1777−1785.

(21) Wang, S.; Li, S.; Chervy, T.; Shalabney, A.; Azzini, S.; Orgiu, E.; Hutchison, J. A.; Genet, C.; Samorì, P.; Ebbesen, T. W. Coherent Coupling of WS2 Monolayers with Metallic Photonic Nanostructures at Room Temperature. Nano Lett. 2016, 16 (7), 4368−4374.

(22) Wen, J.; Wang, H.; Wang, W.; Deng, Z.; Zhuang, C.; Zhang, Y.; Liu, F.; She, J.; Chen, J.; Chen, H.; et al. Room temperature Strong Light-Matter Interaction with Active Control in Single Plasmonic Nanorod Coupled with Two-Dimensional Atomic Crystals. Nano Lett. 2017, 17 (8), 4689−4697.

(23) Liu, W.; Lee, B.; Naylor, C. H.; Ee, H. S.; Park, J.; Johnson, A. T. C.; Agarwal, R. Strong Exciton-Plasmon Coupling in MoS2 Coupled with Plasmonic Lattice. Nano Lett. 2016, 16 (2), 1262− 1269.

(24) Zhu, B.; Chen, X.; Cui, X. Exciton Binding Energy of Monolayer WS2. Sci. Rep. 2015, 5, 9218.

(25) Ramasubramaniam, A. Large Excitonic Effects in Monolayers of Molybdenum and Tungsten Dichalcogenides. Phys. Rev. B: Condens. Matter Mater. Phys. 2012, 86, 115409.

(26) Li, Y.; Chernikov, A.; Zhang, X.; Rigosi, A.; Hill, H. M.; Van DerZande, A. M.; Chenet, D. A.; Shih, E. M.; Hone, J.; Heinz, T. F. Measurement of the Optical Dielectric Function of Monolayer Transition-Metal Dichalcogenides: MoS2MoSe2WS2 and WSe2. Phys. Rev. B: Condens. Matter Mater. Phys. 2014, 90, 205422.

(27) Withers, F.; DelPozo-Zamudio, O.; Schwarz, S.; Dufferwiel, S.; Walker, P. M.; Godde, T.; Rooney, A. P.; Gholinia, A.; Woods, C. R.; Blake, P.; et al. WSe2 Light-Emitting Tunneling Transistors with Enhanced Brightness at Room Temperature. Nano Lett. 2015, 15 (12), 8223−8228.

(28) Zhao, W.; Ghorannevis, Z.; Chu, L.; Toh, M.; Kloc, C.; Tan, P.- H.; Eda, G. Evolution of Electronic Structure in Atomically Thin Sheets of WS2 and WSe2. ACS Nano 2013, 7 (1), 791−797.

(29) Mak, K. F.; Lee, C.; Hone, J.; Shan, J.; Heinz, T. F. Atomically Thin MoS2A New Direct-Gap Semiconductor. Phys. Rev. Lett. 2010, 105, 136805.

(30) Zhang, X. X.; Cao, T.; Lu, Z.; Lin, Y. C.; Zhang, F.; Wang, Y.; Li, Z.; Hone, J. C.; Robinson, J. A.; Smirnov, D.; et al. Magnetic Brightening and Control of Dark Excitons in Monolayer WSe2. Nat. Nanotechnol. 2017, 12 (9), 883−888.

(31) Wurstbauer, U.; Miller, B.; Parzinger, E.; Kormanyos, A.;́ Burkard, G.; Gmitra, M.; Karamatskou, A.; Pearce, A. J.; Burkard, G. Spin−Flip Processes and Radiative Decay of Dark Intravalley Excitons in Transition Metal Dichalcogenide Monolayers. 2D Mater. 2016, 3, 035009.

(32) Arora, A.; Nogajewski, K.; Molas, M. R.; Koperski, M.; Potemski, M. Exciton Band Structure in Layered MoSe2From a Monolayer to the Bulk Limit. Nanoscale 2015, 7, 20769−20775.

(33) Echeverry, J. P.; Urbaszek, B.; Amand, T.; Marie, X.; Gerber, I. C. Splitting between Bright and Dark Excitons in Transition Metal Dichalcogenide Monolayers. Phys. Rev. B: Condens. Matter Mater. Phys. 2016, 93, 121107.

(34) Zhou, Y.; Scuri, G.; Wild, D. S.; High, A. A.; Dibos, A.; Jauregui, L. A.; Shu, C.; DeGreve, K.; Pistunova, K.; Joe, A. Y.; et al. Probing Dark Excitons in Atomically Thin Semiconductors via NearField Coupling to Surface Plasmon Polaritons. Nat. Nanotechnol. 2017, 12 (9), 856−860.

(35) Park, K. D.; Jiang, T.; Clark, G.; Xu, X.; Raschke, M. B. Radiative Control of Dark Excitons at Room Temperature by NanoOptical Antenna-Tip Purcell Effect. Nat. Nanotechnol. 2018, 13, 59− 64.

(36) Wang, G.; Robert, C.; Glazov, M. M.; Cadiz, F.; Courtade, E.; Amand, T.; Lagarde, D.; Taniguchi, T.; Watanabe, K.; Urbaszek, B.; et al. In-Plane Propagation of Light in Transition Metal Dichalcogenide Monolayers: Optical Selection Rules. Phys. Rev. Lett. 2017, 119, 047401.

(37) Vasa, P.; Lienau, C. Strong Light-Matter Interaction in Quantum Emitter/Metal Hybrid Nanostructures. ACS Photonics 2018, 5, 2−23.

(38) Donnell, K. P. O.; Chen, X.; Chen, X. Temperature Dependence of Semiconductor Band Gaps Temperature Dependence of Semiconductor Band Gaps. Appl. Phys. Lett. 1991, 58 (25), 1−4.

(39) Selig, M.; Berghauser, G.; Raja, A.; Nagler, P.; Schu¨ller, C.; Heinz, T. F.; Korn, T.; Chernikov, A.; Malic, E.; Knorr, A. Excitonic Linewidth and Coherence Lifetime in Monolayer Transition Metal Dichalcogenides. Nat. Commun. 2016, 7, 13279.

(40) Moody, G.; Kavir Dass, C.; Hao, K.; Chen, C. H.; Li, L. J.; Singh, A.; Tran, K.; Clark, G.; Xu, X.; Berghauser, G.; et al. Intrinsic¨Homogeneous Linewidth and Broadening Mechanisms of Excitons in Monolayer Transition Metal Dichalcogenides. Nat. Commun. 2015, 6, 8315.

(41) Liu, M.; Pelton, M.; Guyot-Sionnest, P. Reduced Damping of Surface Plasmons at Low Temperatures. Phys. Rev. B: Condens. Matter Mater. Phys. 2009, 79, 035418.

(42) Arora, A.; Koperski, M.; Nogajewski, K.; Marcus, J.; Faugeras, C.; Potemski, M. Excitonic Resonances in Thin Films of WSe2From Monolayer to Bulk Material. Nanoscale 2015, 7, 10421−10429.

(43) Lundt, N.; Marynski, A.; Cherotchenko, E.; Pant, A.; Fan, X.;´ Tongay, S.; Sek, G.; Kavokin, A. V.; Ho¸fling, S.; Schneider, C. Monolayered MoSe2 : A Candidate for Room Temperature Polaritonics. 2D Mater. 2017, 4 (1), 015006.

(44) Zhang, C.; Wang, H.; Chan, W.; Manolatou, C.; Rana, F. Absorption of Light by Excitons and Trions in Monolayers of Metal Dichalcogenide MoS2 Experiments and Theory. Phys. Rev. B: Condens. Matter Mater. Phys. 2014, 89, 205436.

(45) Feist, J.; Garcia-Vidal, F. J. Extraordinary Exciton Conductance Induced by Strong Coupling. Phys. Rev. Lett. 2015, 114, 196402.

(46) Mollow, B. Power Spectrum of Light Scattered by Two-Level Systems. Phys. Rev. 1969, 188 (5), 1969−1975.

(47) Mollow, B. R. Absorption and Emission Line-Shape Functions for Driven Atoms. Phys. Rev. A: At., Mol., Opt. Phys. 1972, 5 (3), 1522−1527.

(48) Zhang, X. X.; You, Y.; Zhao, S. Y. F.; Heinz, T. F. Experimental Evidence for Dark Excitons in Monolayer WSe2. Phys. Rev. Lett. 2015, 115, 257403.

(49) Albrecht, G.; Kaiser, S.; Giessen, H.; Hentschel, M. Refractory Plasmonics without Refractory Materials. Nano Lett. 2017, 17 (10), 6402−6408.

(50) Knight, M. W.; Fan, J.; Capasso, F.; Halas, N. J. Influence of Excitation and Collection Geometry on the Dark Field Spectra of Individual Plasmonic Nanostructures. Opt. Express 2010, 18 (3), 2579−2587.

(51) Johnson, P. B.; Christy, R. W. Optical Constants of the Noble Metals. Phys. Rev. B 1972, 6 (12), 4370−4379.